AIAA

A02-14138

AIAA 2002-0974

FLOW FIELD AND PERFORMANCE OF HIGH FREQUENCY MICROMACHINED SYNTHETIC JETS

Michael O. Müller, Luis P. Bernal,
Peter D. Washabaugh
Department of Aerospace Engineering

Tsung-Kuan Allen Chou, Khalil Najafi
Department of Electrical Engineering
and Computer Science

University of Michigan
Ann Arbor, MI 48109-2140

40th Aerospace Sciences Meeting & Exhibit
14-17 January 2002 / Reno, NV

FLOW FIELD AND PERFORMANCE OF HIGH FREQUENCY MICROMACHINED SYNTHETIC JETS

Michael O. Müller[*], Luis P. Bernal[†], Peter D. Washabaugh[†]
Tsung-Kuan Allen Chou[‡], Khalil Najafi[§]

University of Michigan
Ann Arbor, Michigan 48109-2140

ABSTRACT

The flow field and performance of a new class of micromachined MEMS synthetic jets is characterized using hot wire anemometry, direct thrust measurement and particle image velocimetry. These devices consist of an array of electrostatically driven resonators designed to operate at a resonant frequency of ~70 kHz. Each resonator size is of the order of 1 mm^2 and chips with up to 25 resonators have been fabricated and tested. The effects of drive electrode geometry, and driving frequency and amplitude are documented. The results show that the best performance for a given design is obtained at the system resonance and a voltage slightly above the membrane collapse voltage. These results are in qualitative agreement with previously reported models of the resonators that incorporate the coupled resonance of the acoustic cavity and membrane. It is also shown that there is an optimum electrode geometry that minimizes damping and maximizes performance.

INTRODUCTION

Flow field and performance characterization of a new class of micromachined, electrostatically actuated, synthetic jets are presented in this paper. Figure 1 shows flow visualization of this MEMS synthetic jet. The ultimate goal of the research is the development of high impulse
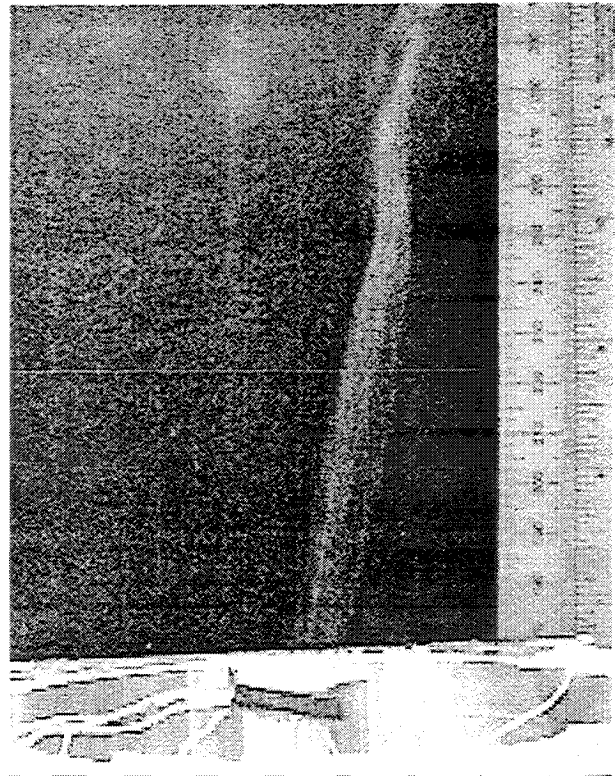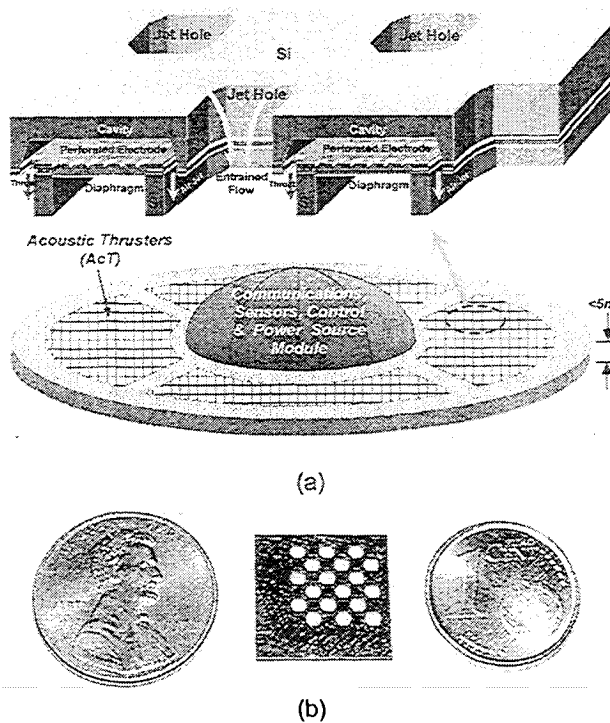

FIGURE 1: Visualization of the flow produced by the micromachined synthetic jet array. The jet outline is visualized by a cloud of ethanol aerosol (heavier than air) introduced below the chip (not shown) and entrained by jets.

micromachined synthetic jets for propulsion of direct-lift ultra-miniature Micro Airborne Platforms. This concept is illustrated in figure 2. Other applications of the technology include integrated microchip cooling devices and integrated micro pumps. Micromachined synthetic jets were first developed by Coe et al.[1,2] for flow control applications. Those jets used piezoelectric and electrostatic drive, and operate at approximately 1.3 kHz.

The micromachined synthetic jets of the present study are electrostatically driven. This

---

[*] Graduate Research Assistant, Department of Aerospace Engineering, Member AIAA.
[†] Associate Professor, Department of Aerospace Engineering, Senior Member AIAA.
[‡] Graduate Student Research Assistant, Department of Electrical Engineering and Computer Science
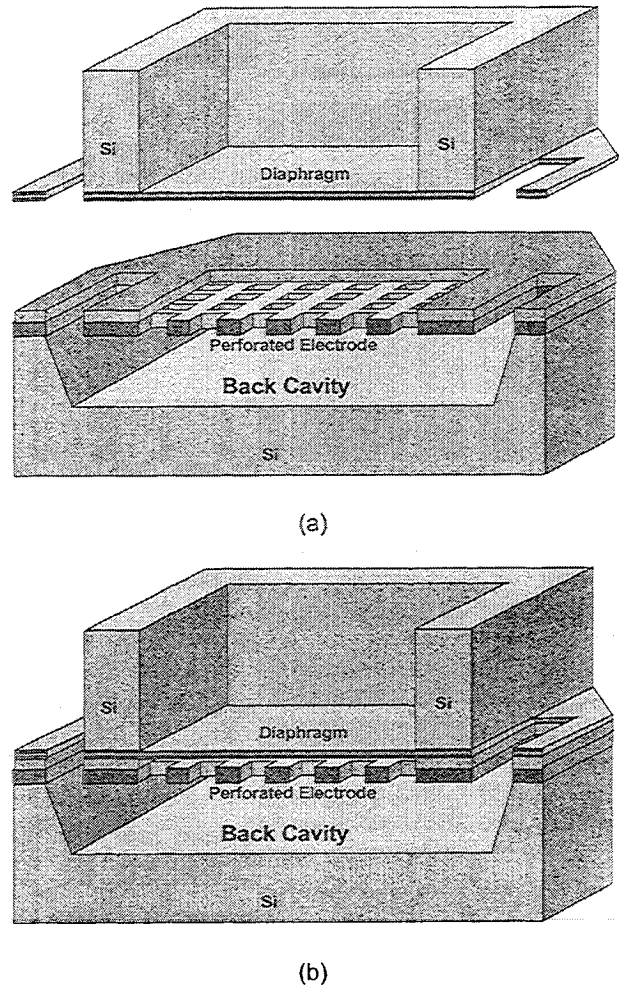[§] Professor, Department of Electrical Engineering and Computer Science.

(a)

(b)

FIGURE 2: Synthetic jet array configured as a direct-lift ultra-miniature Micro Airborne Platform.

(a) Schematic showing array details and overall design concept, including thrusters and mission hardware.

(b) Photograph of a 3 x 6 array adjacent to 1 cent US (left) and 1 cent Euro (right) coins.

(a)

(b)

FIGURE 3: Micromachined synthetic jet construction.

(a) Illustration of individual Silicon wafers. The top wafer contains the diaphragm, the bottom wafer contains the cavity and electrode.

(b) Bonded device. The gap between diaphragm and electrode is defined by bonding material (BCB - Benzocyclobutene).

allows a very compact design: the cavity and drive mechanism are together less than 150 μm thick. The substantial performance required for propulsion is achieved by operating at a very high frequency, approximately 70 kHz. This frequency is above the audible range, ideally suited for many applications where a low noise environment is required. Additional performance can be obtained by integrating the synthetic jets with ejector shrouds to form Micromachined ACoustic Ejectors: "MACE." The MACE devices, as illustrated in figures 2-4, contain an array of resonators distributed around jet holes. Each resonator consists of a cavity and several small throats located around the jet holes[3]. A membrane, driven electrostatically by a perforated electrode located inside the cavity, provides the resonator actuation.

Inherent in these micromachined synthetic jets is the concept of resonance: the jet performance is significantly enhanced when running at resonance. Resonance itself occurs in both the cavity, as an acoustic mode, and in the membrane, as a structural mode. Theoretical models of the

performance of the micromachined synthetic jets have been developed and are used for design optimization[4,5]. Müller et al.[4] describe a reduced order model of synthetic jets driven by an acoustic resonator. They note that the flow topology is asymmetric, the input and output strokes are different for the acoustic cycle. The time-averaged downstream momentum flux introduced in to the flow field is the primary source of thrust. Ignored are the effects of a possibly lower static pressure at the throat, as well as re-ingestion of downstream momentum during the input stroke. A conclusion is the strong performance gains at resonance for a synthetic jet coupled to an acoustic cavity. A large scale test[6] (relative to the
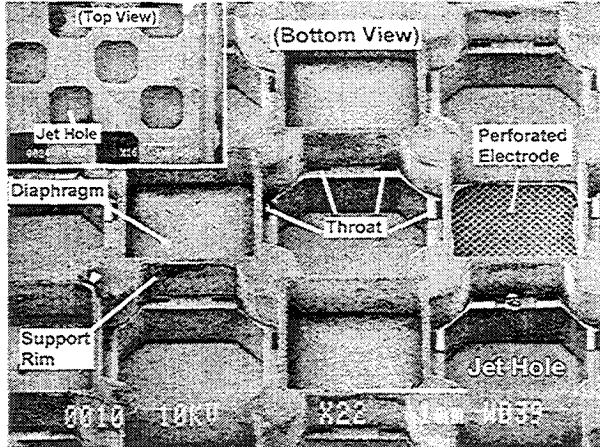
FIGURE 4: Electron microscope image of a completed device showing the jet holes, the throats surrounding the jet holes, and the perforated electrode.

MEMS device) quantified the flow and thrust characteristics of a synthetic jet and validated the results of this model.

Müller et al.[5] study the coupling effects between the resonances of the acoustic cavity and structural membrane. This model demonstrates multiple 'resonances,' which do not coincide with resonances of the separate structural or fluid components. For the micromachined geometry of the present work, two distinct performance maxima are found, each at a fraction of the individual resonant frequencies. The controlling parameter is found to be the ratio of the pressure force on the membrane to its inertia: the thrust performance increases as this ratio decreases. Additionally, increasing the membrane stiffness results in a higher thrust. Thus, for optimum performance, a low inertia, high-tension membrane is desirable.

An important consideration in these MEMS-scale devices is the role of damping in their performance. Viscous damping in the perforated electrode is a major contributor to performance degradation. There are two sources of viscous damping. First, there is viscous damping associated with the flow through the holes. Second, as the membrane collapses the air in the gap is squeezed out and significant pressure build up and damping occurs. In addition, if the electrode width is reduced the electrostatic force acting on the membrane is also reduced which results in performance reduction. Characterization of the effects of electrode design on performance is an important aspect of the present investigation. Viscous effects and acoustic radiation at the resonator throats also contribute to the damping.

These effects have been considered in the models proposed by Müller et al.[4,5] and Parviz et al.[7] Other MEMS-scale manufacturing issues have been studied by Parviz et al.[7] and by Chou et al.[3,8] These previous works serve as a baseline for the present study of MEMS thrusters.

The focus of the present study is to quantify the performance of the micromachined synthetic jets; to investigate the details of the jet qualitatively visualized in figure 1. Flow characterization methods include basic visualization using an ethanol aerosol; detailed velocity measurements using hot wire anemometry; direct thrust measurement using a pendulum arrangement; and flow field measurements using particle image velocimetry (PIV). The device performance is calculated from the velocity measurements. Of interest are the net mass flow (for pumping applications) and the net thrust (for flow control and propulsion applications).

BASIC DESIGN AND CONSTRUCTION

Figures 3 and 4 show the details of the resonator design: several resonators are arranged in a "chess-board" pattern, such that eight throats from four diaphragms surround a jet hole. Each resonator diaphragm drives one cavity with eight throats. There are 18-25 resonators occupying a single device. The device is manufactured using a sandwich of two silicon wafers, in a batch process typical of MEMS manufacturing. The synthetic jet cavity, driving electrode, throats, and the jet hole are etched into one wafer. The diaphragm is manufactured on a second wafer, also containing

Device	Electrode				Resonators per thruster
	L_2 (μm)	L_1 (μm)	% Open area	L_2 / h_o	
A	20	10	11.1	3.3	25
B	25	12	10.5	4.1	25
C	15	7	10.1	2.5	18
D	40	15	7.44	6.7	18

TABLE 1: Geometric dimensions of the devices tested. Figure 5 shows the definition of the parameters L_1 and L_2. Devices C and D are integrated on the same chip.

Throat dimensions: 50 x 200 μm.
Cavity dimensions: 1300 x 1300 x 100 μm.
Electrode thickness: 15 μm.
Electrode to diaphragm distance: $h_o = 6$ μm.
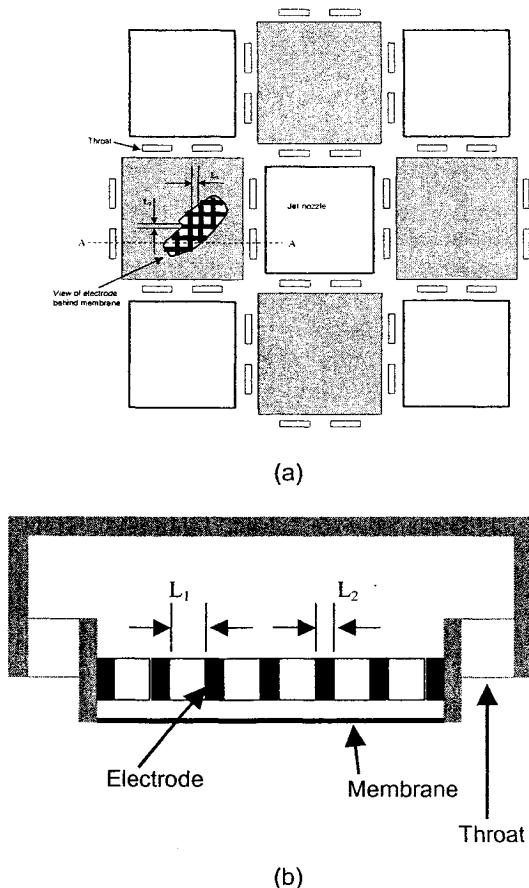
(a)

Electrode   Membrane

Throat

(b)

FIGURE 5: Schematic of individual synthetic jet.
(a) Bottom view, (b) section A – A.

the jet hole. The two wafers are aligned and bonded together to form the array of synthetic jets. Figure 4 is a micrograph of the manufactured device. The image illustrates the arrangement of the jet holes, diaphragms with its support rim, and cavity throats. One diaphragm is removed, showing the perforated electrode underneath.

Table 1 gives the relevant dimensions of the devices tested. The main parameters varied are the size of the electrode holes and the spacing between the holes. Figure 5 illustrates the electrode hole pattern and shows the definition of the parameters L_1 and L_2 listed in table 1. The choice of parameters is such that the open area ratio of the perforations is varies between ~7.5 and ~11, and the ratio of electrode width to diaphragm gap varies by a factor 3. These values were selected in order to clarify the nature of the viscous damping in the electrode.

EXPERIMENTAL METHODS

The nature of the MEMS synthetic jet devices puts constraints on operation, and limits possible testing. The devices are operated with sinusoidal voltages up to 240 V_{pp} and frequencies typically in the range 50-100 *kHz*. The membrane is charged, and the electrode is grounded, creating the driving electrostatic potential. A commercially available signal generator (HP 33120A) and amplifier (Krohn-Hite 7602M) were used to drive the devices.

Several methods were used to characterize the flowfield. Hot wire anemometry was used to measure the mean velocity. The hot wire (TSI model 1210-T1.5) response time is significantly longer than the synthetic jet period, operating at 70 *kHz*. Thus, the hot wire is only used to measure mean jet velocity. The hot wire probe provides a two dimensional average across most of the jet hole. The length of the hot wire is 1270 μm, while the jet hole width is 1500 μm. Thus, the hot wire data is a spatial average over 85% of the hole. However, the hotwire including the supports is considerably wider than the jet hole, preventing measurements inside the jet hole. The "near-field" measurements taken with the hot wire are 10 throat widths (one third of the jet hole width) downstream of the jet hole. For the hot wire data presented here, four realizations are taken around a given jet hole: one above each pair of throats surrounding the jet hole. Figures 6 and 7 show both the range and the mean of data collected. Solid lines indicate the average, and dashed lines indicate the range.

Two image digital PIV measurements were also taken. An ND:YAG laser was used for illumination, and ethanol particles were used as seeding. Proper seeding of the flow is critical. The membranes of the devices tested are exposed, and any substance (solid particles or liquid drops) collecting on them would significantly alter performance, or break, the 2 μm thick membranes. Nebulized high purity ethanol was chosen because of its short evaporation time leaving no residue. The alcohol was injected using four nebulizers, resulting in a short-lived "smoke cloud" with a mean velocity that is two orders of magnitude lower than the flow velocity produced by the devices.

Protecting the devices from the intense laser beam is also critical. Shielding the chip from the intense converging (in one plane) laser beam

required setting the device at an angle such that the diverging (in the second plane) laser beam sheet does not illuminate the chip surface. Thus, the field of view is fully illuminated, but the membranes are shielded from the intense light — including reflections from the highly polished silicon chip surfaces!

RESULTS

Frequency Response

Hot wire anemometry is used to measure the mean throat velocity at constant drive voltage (210 V_{pp}) and varying frequency, as shown in figure 6. Several features of the response are common to all designs. A peak velocity response is observed at about 70 *kHz*, and a smaller second peak at about 110 *kHz*. A fairly large quality factor is evident, as the performance decreases substantially off resonance. The even matching of the resonant frequencies demonstrates that the manufacturing process results in consistent membrane tension and geometric dimensions for all resonators of an individual device. The details of the spectra vary considerably between the various designs, documenting the effect of the electrode design. Device B has consistently higher velocities than the other devices. In contrast device D has the lowest velocities. Also the structure and amplitude of the high frequency peak varies considerably between the different designs. These changes are attributed primarily to the varying damping of the electrode holes. The existence of two distinct maxima is consistent with model predictions for an electrostatically driven synthetic jet[5]. All subsequent results presented here are taken at the frequency corresponding to the peak performance for each design.

Voltage Response

The greatest volume displacement, and thus performance, is achieved when the membrane collapses against the electrode. When the membrane displaces about half the distance to the electrode, the attractive force of the electrode is greater than the restorative force of the membrane tension, and the membrane collapses on to the electrode. By dynamically operating the membrane to the collapse state the volume displaced, and thus performance, is maximized. Figure 7 shows the effect of varying drive voltage on the mean throat velocity in the near field while driving the synthetic jets at the frequency for maximum velocity as discussed above. At low
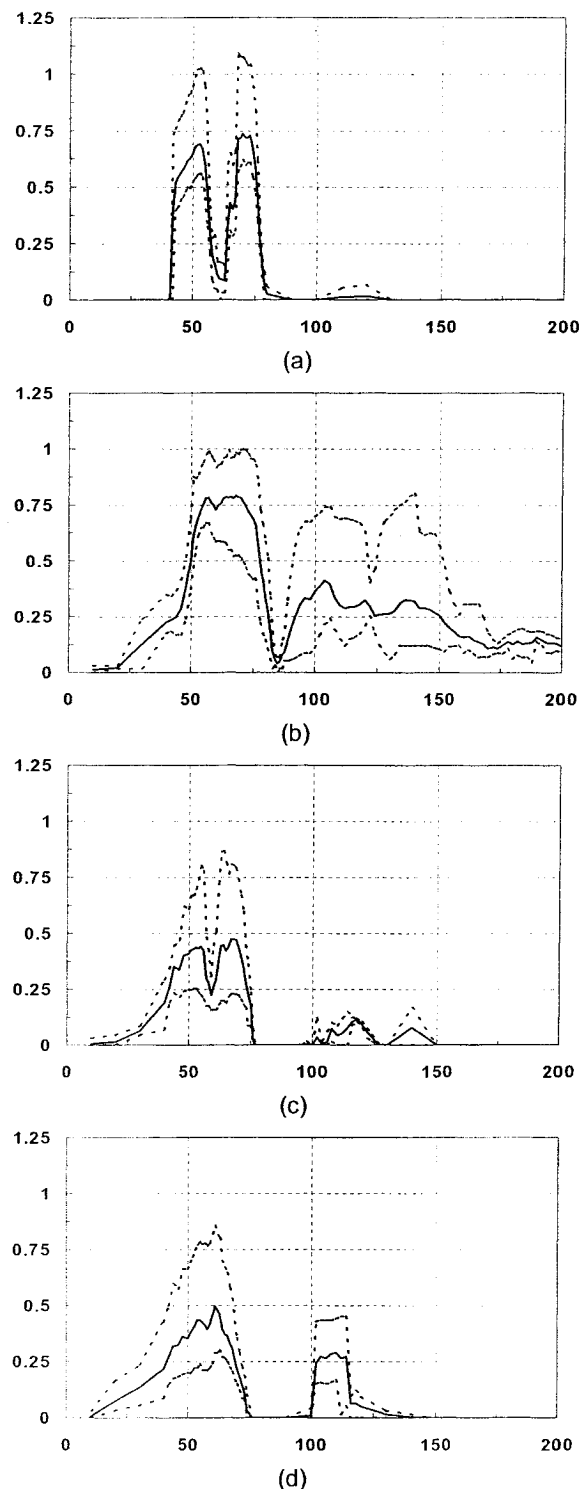

FIGURE 6: Mean velocity above throat at varying membrane frequency, showing resonant behavior. Vertical scale is *m/s*, horizontal scale is *kHz*. Solid line indicates average, dashed lines indicate data range.

(a) Device A, (b) Device B
(c) Device C, (d) Device D

voltages collapse does not occur, i.e. membrane displacement less than half the distance to the electrode, and the measured mean velocity is very low. At some voltage, corresponding the initiation of collapse, the velocity increases very rapidly to a maximum value. Increasing the voltage beyond this value results in only a small increase in the velocity. Figure 7 (a) and (c) show the expected ramp-up associated with the collapse of the membrane against the electrode. In contrast, figure 7 (b) and (d) show a more gradual increase in velocity with voltage. This difference can be attributed to different electrode damping mechanisms. Designs B and D have higher values of the L/h_o parameter indicating that for large L/h_o viscous damping of the flow between the electrode and membrane is dominant, while for small values of L/h_o the viscous damping of the flow through the electrode holes dominates.

These data show that for a given design the best performance is obtained at a voltage just above that required to cause collapse of the membrane. A difference in initial collapse voltage is evident in the four designs, varying from below 60 V to 90 V. These changes could be attributed to differences in damping characteristics as well as electrostatic forcing due to varying electrode designs. For the four cases shown, design B has the best performance in that the maximum mean velocity of ~0.75 m/s is obtained at a lower drive voltage. The low performance of device C is attributed to a reduced electrostatic force.

Mean Flow

Figure 1 shows a flow visualization image of the mean jet flow. A cloud of nebulized ethanol droplets is introduced below the device. The droplets are heavier than air and settle slowly in the absence of the jet. When the device is turned on, the jet entrains the particles and creates the column of droplets visible in the figure. This is design "A", operated at 72 kHz membrane. The jet is more than 10 cm high, significantly larger than the micromachined device itself. A laminar jet is observed with a slow growth rate. There is evidence of instability far away from the device (~7 cm).

Figure 8 (a) shows the peak velocity above a throat at increasing downstream distance for device C operating at 210 V_{pp} and 56 kHz. The results show the expected decay of the maximum velocity with distance. Plotting the inverse of the velocity, in figure 8 (b), the data show an
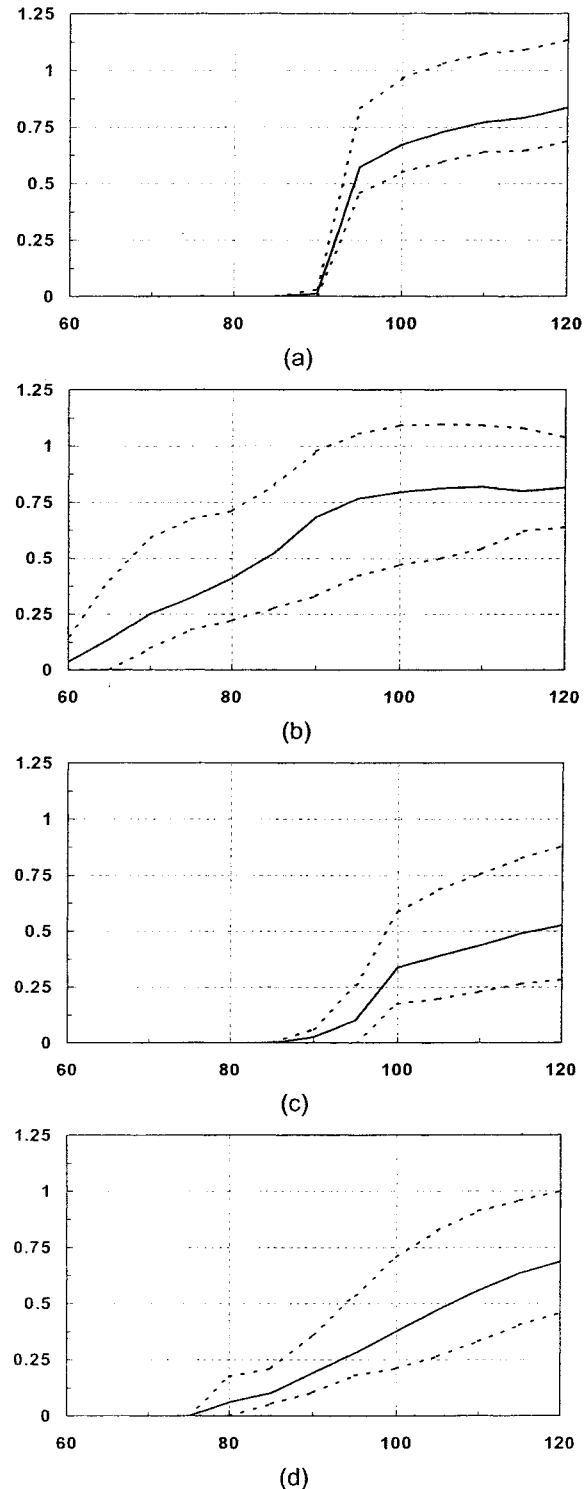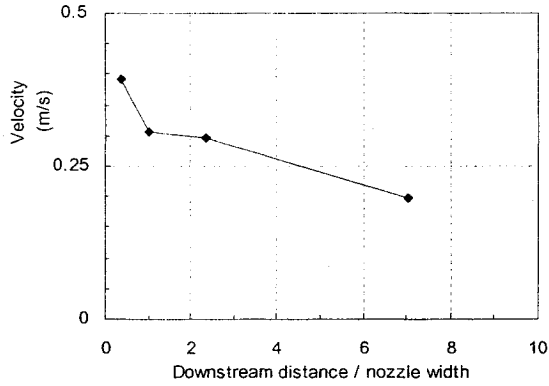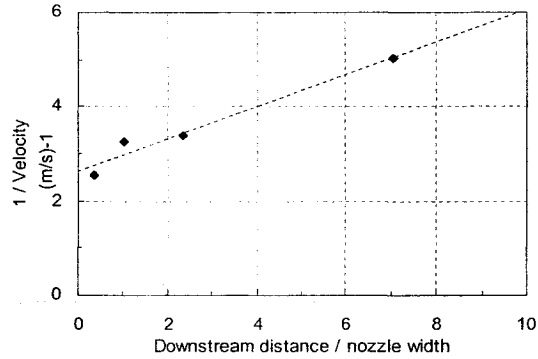

(a)

(b)

(c)

(d)

FIGURE 7: Mean velocity above throat at varying membrane drive voltage. Vertical scale is m/s, horizontal scale is volts. Solid line indicates average, dashed lines indicate data range.
(a) Device A, (b) Device B
(c) Device C, (d) Device D

(a)

(b)

FIGURE 8: Peak velocity above a throat as a function of downstream distance for Design C.

(a) Peak velocity.

(b) Velocity inverse, showing agreement with axisymmetric jet centerline velocity decay.

approximate linear fit as expected for an axisymmetric jet.

Figure 9 shows traverses of the mean velocity field in the nozzle for devices A and C at the frequency for maximum velocity. Data are taken with a hot wire. Evident is significant entrainment between the two throats that results in a considerable non-zero flow velocity at the center of the jet hole. Also evident is a strikingly different shape of the jets of the two devices. This is in part a result of the different momentum fluxes. If we assume the throats (the throats create the flow in the jet hole; see figure 3) create plane laminar jets, the momentum flux J is a function of the mean velocity and jet width,

$$J \propto \overline{u}^2 \, \delta .$$

Taking into account the laminar viscous growth for the jet, we can calculate the momentum ratio as,
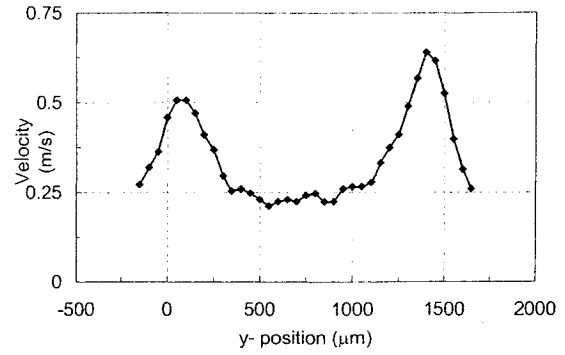
(a)
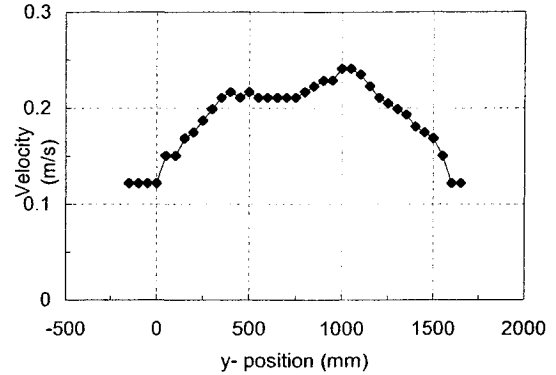
(b)

FIGURE 9: Traverse of velocity field of single jet hole showing entrainment.
The throats are located at 0-50 and 1450-1500 μm.
(a) Design A
(b) Design C

$$\frac{J_A}{J_B} = \frac{\overline{u}_A^{3/2}}{\overline{u}_B^{3/2}} = 2.4 .$$

Finally, the jet width is a function of downstream distance and momentum,

$$\delta \propto \frac{x^{2/3}}{J^{1/3}} .$$

These simple scaling arguments suggest that the downstream growth of the jets emanating from the throats of design A is smaller by 30% compared to the jet produced by design B devices. In figure 9 (b), the jets have merged, while in figure 9a they are still separate. The location of the maximum velocity has moved towards the jet center in design C. These differences cannot be attributed only to the different growth rates of the laminar free jets. Another contributing factor is the

7

American Institute of Aeronautics and Astronautics
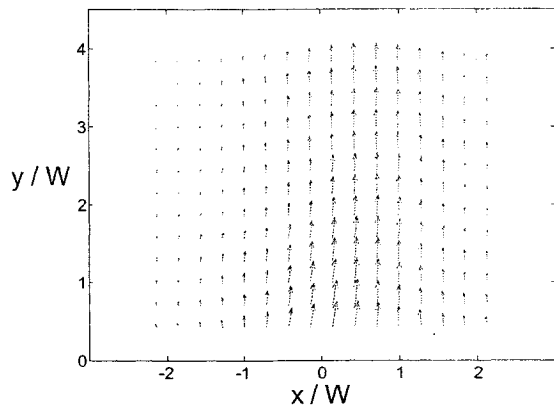
FIGURE 10: PIV-measured flow field for a design A jet hole. Axes normalized with jet hole width, W.

Nozzle located at –0.5 < x/W < 0.5, y/W = 0.

Maximum velocity in the field: 0.47 *m/s*.

(a)

(b)

FIGURE 11: Illustration of the thrust measurement results. A device weighting 0.59 *g* is suspended on a 43 *cm* long pendulum. When the device is turned on a 2 *mm* displacement is observed, which corresponds to a thrust of 27 μN.

(a) Device "off" condition
(b) Device "on" condition

influence of the wall that must also be taken into account in the analysis.

Figure 10 shows the simultaneous flow field, as measured using PIV. The field of view is about 7 by 7 *mm*, corresponding to 4.5 jet hole widths on a side. The PIV measured peak velocity, 0.5 *m/s*, agrees with the hot wire results. The PIV image is processed at a relatively low spatial resolution, and the details of the unsteady flow structure are not captured.
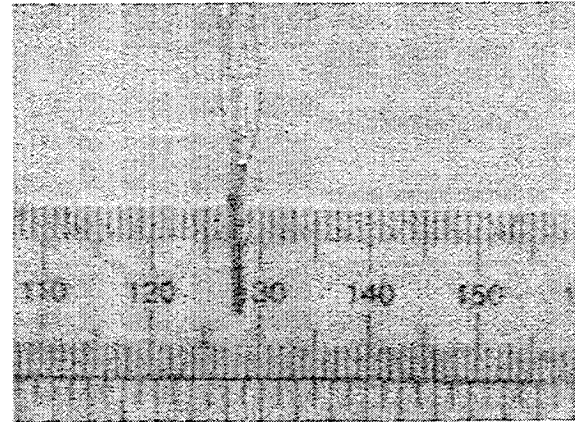
Performance

Direct thrust measurement of device B is shown in figure 11. The device containing 25 synthetic jets directed towards the left of the figure is suspended on a pendulum. Figure 11 (a) shows the equilibrium position with the device turned off. Figure 11 (b) shows the equilibrium position with the device turned on. Thrust causes the equilibrium position to shift to the right by 2 *mm* as measured with the ruler. From the pendulum length and device weight, a thrust of 27 μN is calculated. The measurement uncertainty of the direct thrust measurement is 25%. As shown by the velocity data there is considerable variability among the various devices and throats on the same chip.
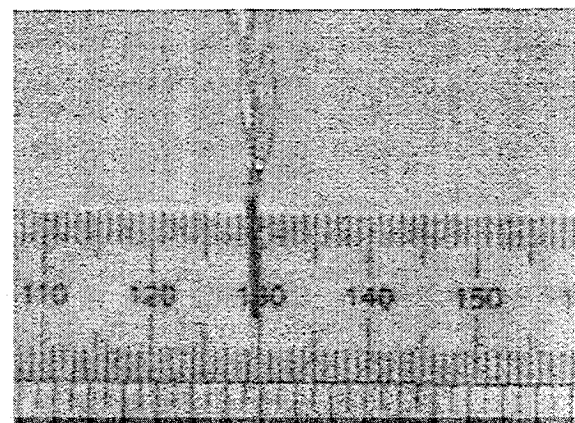
Given the velocity data across a nozzle, the mass flow and thrust can be calculated as,

$$\dot{m} = \rho u dA$$

$$Th = \rho u^2 dA .$$

Using the spatial average velocity from the hot wire traverse and the PIV data, the thrust can also be obtained. Table 2 shows the performance of design A calculated using the three techniques. There is reasonable agreement in the three results. The discrepancies of the data shown in Table 2 are consistent with the uncertainty of the techniques used (~25%).

In reviewing these results, the mass of the device is about 9 *g*, requiring 8.8 *mN* of thrust for direct lift. This is several orders of magnitude higher than the presently measured values! However, thrust scales as the square of the velocity, which in turn scales linearly with membrane displacement and operating frequency. New technologies are being developed to bring

8

American Institute of Aeronautics and Astronautics

	HW Calculated	PIV Calculated	Direct Measurement
Mass Flux, mg/s	23.7	19.7	N / A
Thrust, μN	8.2	5.7	10

TABLE 2: Mass flow and thrust measurements for design A.

about at least an order of magnitude increase in membrane deflection[9]. Additionally, the use of ejector and inlet shrouding will provide a significant thrust augmantation.

CONCLUSION

The primary objective of the development of micromachined acoustic resonators is to design and manufacture synthetic jets that provide practical levels of thrust. The underlying design concept is to operate the micro thrusters at the largest possible frequency and membrane displacement to maximize the thrust produced. Theoretical analyses reported elsewhere[4-7] show that the maximum performance is determined by the resonant characteristics of the coupled acoustic and structural components. For the present electrostatically driven membranes, the maximum membrane displacement is determined by the distance between the electrode and membrane. The results presented here are in agreement with these models. The maximum performance is obtained at a well-defined frequency and above a voltage threshold associated with the collapse of the membrane.

The present measurements show the effects of electrode perforation design in the performance of the devices. It is shown that there is an optimum ratio of L/h_0 of the order of approximately 4, for an open area ratio of 10%. Smaller values result in increased damping associated with pressure drop through electrode perforations and possibly reduced electrostatic force. Larger values also result in reduced performance due to the higher viscous damping as the fluid is ejected between the diaphragm and electrode.

Measurements of the jet hole flow show a well-defined jet structure. At sufficiently high momentum two distinct peaks in the velocity are found. These are associated with the jets produced by the narrow resonator throats. At lower momentum there is a more rapid growth, and the individual jets merge closer to their origin.

Mass entrainment for a typical device is found to be 20 mg/s and the thrust 10 μN, which suggests a power to thrust ratio of approximately 0.2 W/N. It is interesting to use these results to calculate the power to thrust ratio for a device with an order of magnitude increase in performance. The extrapolated value of power to thrust ratio is of the order 2 W/N.

In concluding, we note that the detailed analysis of these new devices requires the development of experimental methodology. In this paper, traditional measurement techniques are applied to unconventional geometries and devices. New experimental techniques need to be developed to better quantify the very small scale, very large frequency parameter range characteristic of the MACE micromachined thrusters.

REFERENCES

[1] COE, D.J., ALLEN, M.G., TRAUTMAN, M.A. AND GLEZER, A. 1994 Micromachined jets for manipulation of macro flows. Solid-State Sensor and Actuator Workshop, Hilton Head, South Carolina, June 13-16.

[2] COE, D.J., ALLEN, M.G., SMITH, B. L. AND GLEZER, A. 1995 Addressable micromachined jet arrays. Transducers 1995.

[3] CHOU, T.-K.A., NAJAFI, K., MÜLLER, M.O., BERNAL, L.P. AND WASHABAUGH, P.D. 2001 High density micromachined acoustic ejector arrays for micro propulsion. Transducers 2001.

[4] MÜLLER, M.O., BERNAL, L.P., MORAN, R.P., WASHABAUGH, P.D., PARVIZ, B.A. AND NAJAFI, K. 2000 Micromachined acoustic resonators for microjet propulsion. AIAA Paper 2000-0547.

[5] MÜLLER, M.O., BERNAL, L.P., MORAN, R.P., WASHABAUGH, P.D., PARVIZ, B.A., CHOU, T.-K.A., ZHANG, C. AND NAJAFI, K. 2000 Thrust performance of micromachined synthetic jets. AIAA Paper 2000-2404.

[6] MÜLLER, M.O., BERNAL, L.P., MISKA, P.K., WASHABAUGH, P.D., CHOU, T.-K.A., PARVIZ, B.A., ZHANG, C. AND NAJAFI, K. 2001 Flow structure and performance of axisymmetric synthetic jets. AIAA Paper 2001-1008.

[7] PARVIZ, B.A., CHOU, T.-K.A., ZHANG, C., NAJAFI, K., MÜLLER, M.O., BERNAL, L.P. AND WASHABAUGH, P.D. 2000 A wafer integrated array of micromachined electrostatically-driven ultrasonic resonators for microfluidic applications. Proceedings of IEEE International MEMS Conference, Miyazaki, Japan.

[8] CHOU, T.-K.A., NAJAFI, K.N. 2001 3D MEMS fabrication using low temperature wafer bonding with Benzocyclobutene (BCB). Transducers 2001.

[9] CHOU, T.-K.A., NAJAFI, K.N. 2002 Fabrication of out-of-plane curved surfaces in Si by utilizing RIE lag. To be presented, IEEE International MEMS Conference, Las Vegas, USA.